Advanced Materials

ADVANCED MATERIALS
www.advmat.de

RESEARCH ARTICLE

Promoted CO_2 Electrolysis to Formic Acid Using Single Atom Cobalt Alloyed Tin

Jing Xue[1,2] | Bifa Ji[3] | Kexin Zhong[2] | Yizhen Chen[4] | Xu Li[2] | Jiawei Li[5] | Chunxiao Liu[2] | Qunxiang Li[1] | Jie Zeng[1,6] | Tingting Zheng[2] | Yongping Zheng[7] | Chuan Xia[2]

[1]Hefei National Research Center For Physical Sciences At the Microscale, University of Science and Technology of China, Hefei, Anhui, P. R. China | [2]School of Materials and Energy, University of Electronic Science and Technology of China, Chengdu, P. R. China | [3]Advanced Energy Storage Technology Research Center, Shenzhen Institute of Advanced Technology, Chinese Academy of Sciences, Shenzhen, P. R. China | [4]Department of Chemical Engineering, University of California, Davis, California, USA | [5]School of Materials Science and Engineering, Nanyang Technological University, Singapore, Singapore | [6]School of Chemistry & Chemical Engineering, Anhui University of Technology, Ma'anshan, Anhui, P. R. China | [7]Guangdong Provincial Key Laboratory of New Energy Materials Service Safety, College of Materials Science and Engineering, Shenzhen University, Shenzhen, P. R. China

Correspondence: Jie Zeng (zengj@ustc.edu.cn) | Tingting Zheng (ttzheng@uestc.edu.cn) | Yongping Zheng (ypzheng@szu.edu.cn) | Chuan Xia (chuan.xia@uestc.edu.cn)

Received: 28 November 2025 | **Revised:** 2 February 2026 | **Accepted:** 20 February 2026

Keywords: CO_2 reduction reaction | formate/formic acid | single atom alloy | porous solid electrolyte reactor

ABSTRACT

Electrochemical CO_2 reduction with renewable electricity offers a promising path for accessing carbon-neutral liquid chemicals. Although post-transition metals, especially tin (Sn), are intrinsically selective for formate, most catalysts still require high overpotentials to reach industrially relevant current densities and lose activity under sustained operation. Here, we report a single-atom alloy catalyst, comprising isolated cobalt (Co) atoms in a Sn matrix (Co_1Sn), that drives CO_2-to-formate with near-unity selectivity at high rates. Co_1Sn achieves an $FE_{formate}$ of up to 99% at current densities exceeding −1 A cm^{-2}. At current densities ranging from −100 to −1000 mA cm^{-2}, Co_1Sn maintained >92% formate selectivity. When integrated in a porous solid electrolyte reactor, a continuous production of pure formic acid was enabled for 130 h at a current density of −50 mA cm^{-2} with an FE_{HCOOH} of ∼95%. In situ spectroscopy and theoretical simulation demonstrated that the incorporation of single Co atoms finely tuned the electronic structure of the Sn matrix, enhanced CO_2 activation, and lowered barriers along the O-bound *OCHO pathway, thereby facilitating formate generation. This work resolves the rate-selectivity-durability trade-off in formic acid electrosynthesis by leveraging a single-atom alloying strategy.

1 | Introduction

The electrochemical reduction of carbon dioxide (CO_2RR) is a promising approach to mitigate climate change by closing the carbon loop and producing value-added chemicals using renewable electricity [1–3]. Among the possible CO_2RR products, formic acid (HCOOH), often obtained as formate ($HCOO^-$) in solution, stands out as particularly attractive due to its wide range of industrial applications and favorable energy economics [4–6]. Formic acid is used extensively in pharmaceutical synthesis, agriculture, leather processing, and electrolytic metal refining, and it has even been proposed as a hydrogen carrier (containing ∼53 g H_2 per liter) for fuel cells [7]. Its high market value relative to its energy content (on a cents per kWh basis) makes HCOOH one

Jing Xue and Bifa Ji contributed equally to this work.

of the most economically viable products from the CO_2RR. These considerations have driven substantial interest in developing efficient electrocatalysts for CO_2-to-formate conversion.

Many post-transition (*p*-block) metals are known to catalyze the CO_2RR toward formate with high selectivity. In particular, tin (Sn), bismuth (Bi), indium (In), lead (Pb), and mercury (Hg) electrodes favor the production of formate/formic acid over CO or hydrocarbon products [8–13]. Among these materials, Sn-based materials have emerged as especially promising formate producers owing to their low cost, earth abundance, and relative environmental benignity [14–17]. On Sn surfaces, stabilization of the O-bound *OCHO intermediate facilitates the first proton-coupled electron transfer to CO_2 and promotes formate formation [18, 19]. However, pristine Sn catalysts still suffer from several critical limitations that hinder their practical application. Notably, the subsequent reduction of *OCHO to formate requires a high thermodynamic driving force on Sn, leading to large overpotentials and low energy efficiencies [18, 20, 21]. Sn also binds *COOH and *H intermediates only moderately, which means that competing pathways to CO and H_2 are not fully suppressed [18]. As a result, typical Sn electrodes achieve faradaic efficiencies (FEs) for formate on the order of ∼80%–85% under optimal conditions, with the remainder lost to H_2/CO byproducts [22–24].

One promising strategy to overcome these limitations is to finely tune the surface chemistry of the catalyst via single-atom alloying. By incorporating isolated heteroatoms into a host metal matrix, one can modulate local electronic states and adsorption energetics with atomic precision while avoiding secondary phases and maximizing metal utilization [6, 25, 26]. The presence of a heterogeneous metal atom in the local environment can alter the binding energy of intermediates such as *OCHO and *COOH, which in turn boosts activity and selectivity [27]. For instance, doping *p*-block metals with a small amount of transition metal has been reported to shift the *p*-band center of the host closer to the Fermi level, facilitating CO_2 adsorption and activation [28]. Cobalt (Co) is an attractive dopant, being a low-valence 3*d* transition metal with an electron-deficient character that withdraws electron density from the Sn lattice [28, 29]. We therefore anticipate that isolated Co atoms embedded in the Sn matrix would induce charge transfer and electronic perturbations that promote CO_2 reduction to formate.

Herein, we present a Co_1Sn single-atom alloy (SAA) catalyst, featuring Co atoms atomically dispersed in a Sn matrix, that achieves highly efficient and selective conversion of CO_2 to formic acid. The Co_1Sn catalyst demonstrates an outstanding formate selectivity > 92% (up to 99%) across a wide cathode potential window (from −0.83 to −1.33 V vs a reversible hydrogen electrode, RHE), while delivering current densities of up to −1000 mA cm^{-2}. In situ spectroscopic analysis and density functional theory calculations reveal that the incorporated Co atoms help to activate CO_2 and optimize the energetics of the reaction intermediates (CO_2^- and *OCHO), lowering the energy barrier for formate formation. When integrated into a porous solid-state-electrolyte (PSE) reactor, the Co_1Sn SAA exhibits remarkable long-term stability, continuously producing pure formic acid over >130 h of operation at a current density of −50 mA cm^{-2} with an FE_{HCOOH} of approximately 95%.

2 | Results and Discussion

The Co_1Sn SAA catalyst was prepared through a facile one-step reduction of metal chlorides with $NaBH_4$ (see the Supporting Information). Powder X-ray diffraction (PXRD) shows reflections indexed to tetragonal Sn (PDF 86–2264) with no additional peaks attributable to Co-containing phases (Figure 1a), excluding crystalline Co clusters within the detection limit. Transmission electron microscopy revealed nearly spherical particles with diameters of 60–100 nm (Figure S1). High-angle annular dark-field scanning transmission electron microscopy (HAADF-STEM) image combined with energy-dispersive X-ray spectroscopy (EDS) mapping (Figure 1b; Figures S2 and S3) revealed that a spatially uniform Co signal colocalized with Sn across the particles. The concentration of the Co component of the as-synthesized sample was ca. 1.0 at%, as determined by inductively coupled plasma-atomic emission spectroscopy (ICP-AES). X-ray photoelectron spectroscopy (XPS) reconfirmed the presence of Sn and Co (Figure S4), with a slight degree of surface oxidation. The above results, taken together, demonstrate that Co was homogeneously distributed in the Sn matrix, which is consistent with a single-atom alloy.

To resolve the local coordination and electronic state of Co under reaction conditions, we carried out in situ X-ray absorption spectroscopy (XAS) during the CO_2RR. Figure 1c shows the Co *K*-edge normalized absorption spectra of the Co_1Sn catalyst under different applied potentials, with Co foil as a reference. The Co *K*-edge X-ray absorption near-edge structure (XANES) of Co_1Sn at the open-circuit potential closely matches that of metallic Co, in accordance with *ex situ* characterization. Upon applying increasingly negative potentials, XANES featured a slight edge shift to lower energy, which was consistent with an increase in electron density at Co sites (Figure 1c; Figure S5, detailed data processing procedures are provided in the Supporting Information). Extended X-ray absorption fine structure (EXAFS) analysis further confirmed the single-atom configuration. The Fourier-transformed EXAFS spectra exhibited a dominant shell at ∼2.66 Å assignable to Co-Sn scattering across the entire potential range (Figure 1d,e; Figure S6 and Table S1) [30]. Quantitative fitting yielded Co-Sn coordination without any detectable Co-Co contribution near ∼2.49 Å (Figure S7 and Table S2) [31]. The absence of a Co-Co path, combined with PXRD and STEM/EDS, excludes Co aggregation within the sensitivity of these techniques and verifies that Co remains atomically dispersed in the Sn lattice during operation. We next assessed how Co incorporation perturbs the Sn electronic structure. Ultraviolet photoelectron spectroscopy (UPS) showed a measurable shift in the valence-band center and work function relative to those of pristine Sn upon Co addition (Figure 1f). The downshift of the Sn *p*-band center evidenced charge transfer from Sn to Co. This result established charge redistribution between Sn and Co, providing a mechanistic basis for the formate-selective activity described below.

The catalytic CO_2RR activities of the Co_1Sn and pristine Sn catalysts were evaluated in a standard three-electrode flow cell system with 0.5 M $KHCO_3$ as the electrolyte (see Methods and Figure S8). The gas products were analyzed by gas chromatography (GC), and the liquid products were analyzed via ion

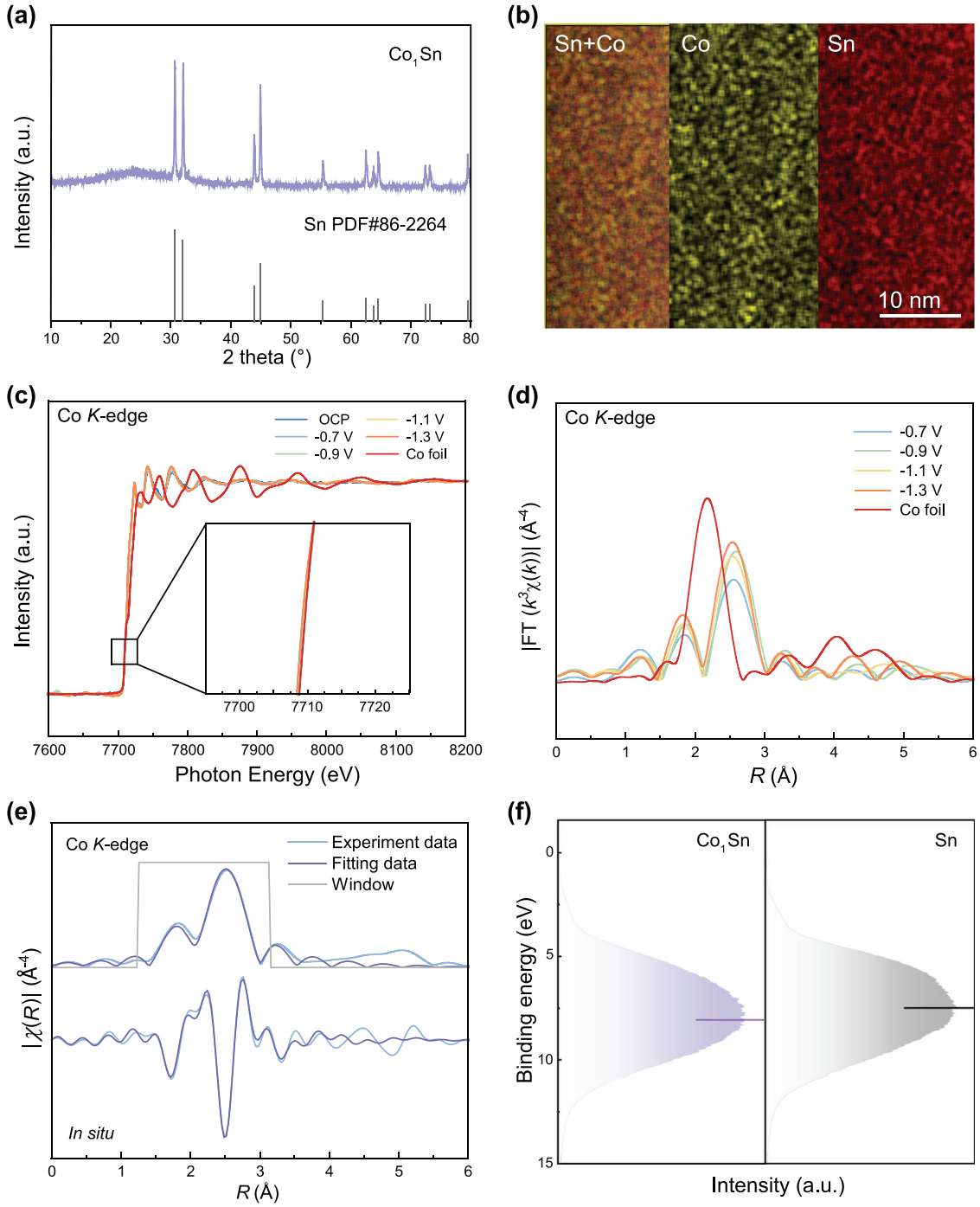

FIGURE 1 | Structural characterization of the Co_1Sn catalyst. (a) PXRD characterization profile. (b) HAADF STEM-EDS mapping of Sn and Co. The full image is provided in Figure S3. (c,d) In situ XAS and EXAFS spectra of the Co_1Sn catalyst under applied potentials during the CO_2RR. All potentials were calibrated to the RHE scale. (e) Detailed in situ EXAFS simulation (k^2-weighted) of the Co_1Sn catalyst at −0.9 V versus RHE. Fourier transforms were performed over a k range from 2.50 to 8.80 $Å^{-1}$ using a Hanning window, while the R range was 1.25–3.15 Å. f) UPS spectra of the pristine Sn and Co_1Sn catalysts.

chromatography (IC) and nuclear magnetic resonance (NMR) spectroscopy. For both catalysts, formate was the only liquid product detected (Figure S9), whereas minor amounts of H_2 and CO were observed in the gas phase (Figure 2a). Co_1Sn delivered near-exclusive formate production over a broad operating window. The maximum faradaic efficiency for formate ($FE_{formate}$) reached 99% at −0.89 V versus RHE with a current density of −200 mA cm^{-2}. Across current densities from −100 to −1000 mA cm^{-2}, $FE_{formate}$ remained above 92% (up to 99%) over potentials ranging from −0.83 to −1.33 V versus RHE (Figure 2a,b). Even at −1 A cm^{-2} (−1.33 V vs RHE), Co_1Sn maintained a formate FE of approximately 93%, indicating robust selectivity at technically relevant rates. In contrast, pristine Sn required more negative bias to approach peak selectivity and performed less selectively overall: its highest $FE_{formate}$ was ~92% at −1.23 V versus RHE, and hydrogen evolution became pronounced at

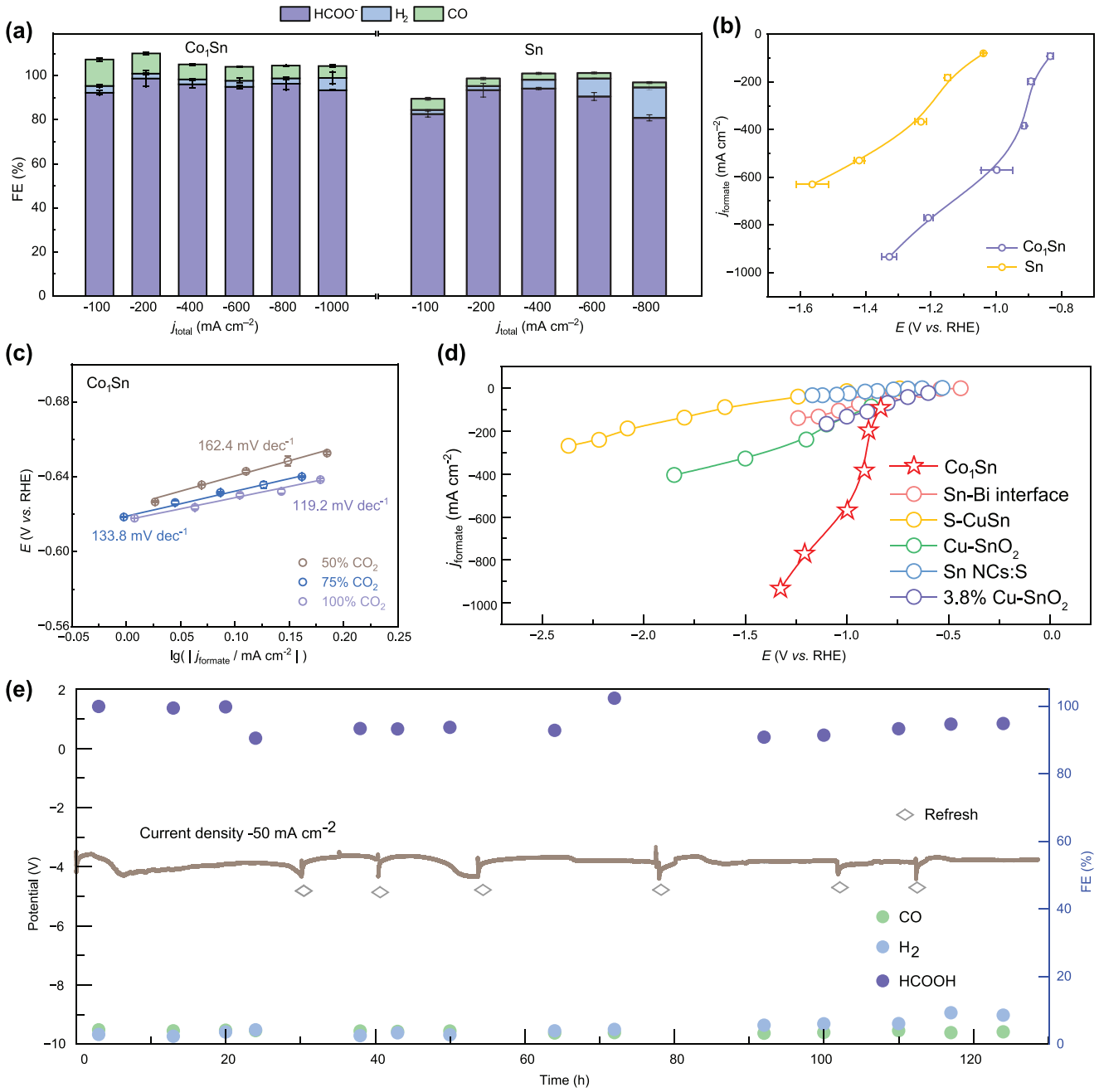

FIGURE 2 | CO_2RR performance of the Co_1Sn and Sn catalysts. (a) FEs of all CO_2RR products at different current densities. (b) $j_{formate}$-V curves of the two catalysts. The error bars in (a,b) correspond to the standard deviation of three independent measurements with 0.5 M $KHCO_3$ as the electrolyte. (c) Tafel slopes for the Co_1Sn catalyst at different CO_2 partial pressures. (d) $j_{formate}$-V curves of the state-of-the-art Sn-based catalysts in flow cell systems during the CO_2RR compared with those of the Co_1Sn catalyst. Catalyst references reproduced from the Sn-Bi interface [15], S-CuSn [32], Cu-SnO_2 [33], Sn NCs:S [34], and 3.8% Cu-SnO_2 [35]. (e) Stability test of the Co_1Sn catalyst at a current density of −50 mA cm^{-2} in a PSE reactor without *iR* corrections.

elevated current densities. Partial current density-potential plots for formate underscore the reduced overpotential and enhanced CO_2-to-formate conversion on Co_1Sn relative to Sn ($j_{formate}$-V, Figure 2b). During the CO_2RR, the CO fraction in the gas phase was modestly greater for Co_1Sn (approximately 5–12%) than for Sn (approximately 2–5%) while $FE_{formate}$ remained dominant. This disparity is probably derived from the incorporation of the Co dopant, which tunes the electronic structure of the Sn matrix and consequently influences its catalytic properties. To eliminate the potential influence of the electrochemically active surface area (ECSA), we quantified the ECSA from the double-layer capacitance measured in the nonfaradaic region and normalized the currents accordingly (Figure S10). After ECSA normalization, Co_1Sn still exhibited larger $j_{formate}$ at identical potentials than pristine Sn did (Figure S11), confirming that the performance advantage arises from intrinsic catalytic enhancement rather than surface area effects.

In situ differential electrochemical mass spectrometry (DEMS) was employed to track the onset potentials of the gas product

during the CO_2RR process on both catalysts. As shown in Figure S12, CO evolution appears at less negative potentials on Co_1Sn and increases steadily in concentration, which is consistent with the slightly higher CO faradaic efficiencies observed in Figure 2a. To assess the reaction kinetics for CO_2-to-formate conversion, we conducted Tafel analysis (Figure S13). Co_1Sn exhibits a Tafel slope of 119.2 mV dec^{-1}, which is markedly smaller than that of pristine Sn (288.5 mV dec^{-1}), suggesting faster reaction kinetics on the Co-modified surface. In the context of the CO_2RR, a Tafel slope near 118 mV dec^{-1} generally implies that electron transfer to CO_2 is the rate-determining step (RDS) (Table S3) [36, 37]. Since practical Tafel measurements can be influenced by transport and data processing, we further examined Co_1Sn under various CO_2 partial pressures. In the kinetic regime, the Tafel slope increased from 119.2 to 162.4 mV dec^{-1} as the CO_2 partial pressure decreased (Figure 2c), supporting the conclusion that CO_2 participates in the RDS and that CO_2 adsorption/activation sensitivity underpins the observed kinetics [38].

To benchmark the catalytic performance, we compared Co_1Sn with state-of-the-art Sn-based catalysts reported in neutral electrolytes [15, 32–35]. As depicted in Figure 2d, Co_1Sn achieved higher current densities at lower overpotentials than previously reported counterparts. We then evaluated structural robustness and device-level durability in a porous solid electrolyte (PSE) reactor configured for pure formic acid production (Figure S14). The Co_1Sn catalyst sustained an FE_{HCOOH} of ~95% for 130 h at a constant current density of −50 mA cm^{-2} without discernible voltage decay (Figure 2e). An average concentration of ~0.028 M pure formic acid solution was demonstrated in the PSE reactor at approximately 4.0 V (Figure S15). In addition, the Co_1Sn catalyst delivered a maximum full-cell energy efficiency of 48% from electricity to pure formic acid. Overall, this performance in producing pure formic acid is competitive with the performance of representative state-of-the-art In/Bi-based catalysts reported in comparable PSE configurations (Table S4), highlighting the high selectivity and operational stability of Co_1Sn for practical CO_2-to-HCOOH electrosynthesis. In addition, post-operation characterization by HAADF-STEM EDS and large-area EDS showed that the single-atom alloy morphology was preserved, with Co remaining homogeneously dispersed in the Sn matrix (Figures S16 and S17). Elemental mapping did not reveal a resolvable change in the ratio of Sn to Co after the 130 h test (Figure S18). To further verify the structural robustness of this single-atom alloy, we conducted XAS analysis after electrolysis. As depicted in Figures S19 and S20 and Table S5, the post-reaction EXAFS profile of Co_1Sn presented only Co-Sn coordination at 2.66 Å without a Co-Co contribution, proving that Co sites remain atomically dispersed after electrolysis. Taken together, these results establish Co_1Sn as a durable and intrinsically active electrocatalyst for CO_2-to-HCOOH conversion.

To elucidate the CO_2-to-formate conversion pathway, we conducted in situ Raman spectroscopy on pristine Sn and Co_1Sn during a cathodic sweep from −0.3 to −1.2 V versus RHE (Figure 3a,b). Both catalysts exhibited two bands at ~1160 and ~1540 cm^{-1}, assignable to carboxylate species associated with formate formation during the CO_2RR [39, 40]. These bands were substantially more intense for Co_1Sn, whereas weaker signals appeared for Sn at more negative potentials, indicating a higher surface coverage and/or production rate of formate-related intermediates on the Co-modified surface. For both catalysts, the band intensities rose and then decayed as the potential approached −1.2 V versus RHE, which was consistent with the progressive consumption/desorption of formate intermediates. Notably, at −1.2 V versus RHE, the carboxylate signal remained detectable on Co_1Sn but was nearly absent on Sn, further evidencing facilitated formate formation on Co_1Sn. The band at ~1010 cm^{-1} derived from the $\nu(HCO_3^-)$ vibration was observed for both catalysts during the CO_2RR [41, 42]. An additional band at ~1060 cm^{-1}, attributed to the $\nu(CO_3^{2-})$ vibration [41, 42], emerged at less negative potentials on Co_1Sn. After the peak areas of these two species on pristine Sn and Co_1Sn were integrated, the ratios of CO_3^{2-}/HCO_3^- under different cathodic potentials were determined and are summarized in Figure S21. It has been reported that a relatively high concentration of CO_3^{2-} is associated with a relatively alkaline interfacial environment [43, 44], a condition that correlates with suppressed hydrogen evolution and a relatively high $FE_{formate}$ for Co_1Sn (Figure 2a). In addition, to verify that the Sn phase remained metallic under operating conditions, we monitored the Sn-O Raman signature. No band near ~630 cm^{-1} (symmetric Sn-O stretching) was detected for Co_1Sn (Figure S22) [13, 33, 45], suggesting that the Sn phase of Co_1Sn remained stable during the reaction.

Complementary in situ attenuated total reflectance surface enhanced infrared absorption spectroscopy (ATR-SEIRAS) further resolved surface intermediates (Figure 3c,d). Upon stepping from −0.6 to −1.3 V versus RHE, an infrared band at 1410 cm^{-1} appeared for both catalysts, which was associated with the O-C-O vibration of *OCHO [20, 46]. Under the same background intensity and signal-to-noise ratio, the band intensity of *OCHO intermediates was higher for Co_1Sn, suggesting greater surface coverage of the adsorbed formate upon Co incorporation into Sn. These ATR-SEIRAS spectra corroborate the in situ Raman results, demonstrating facilitated formate generation on the Sn matrix of Co_1Sn.

To rationalize the enhanced CO_2RR activity on Co_1Sn, we further performed density functional theory (DFT) calculations. The Sn host was modeled in the tetragonal $I4_1/amd$ structure; the simulated diffraction pattern (Figure S23) is consistent with the experimental PXRD data (Figure 1a). The surface energetics were evaluated for low-index terminations, followed by full relaxation. The (001) facet undergoes mild reconstruction and has a lower surface energy by ~0.01 eV $Å^{-2}$ than the (100) and (010) facets (Figure S24). Accordingly, (001) was taken as the predominant exposed surface and as the host for isolated Co atoms.

In near-neutral or alkaline electrolytes, the proton source is water, so hydrogen delivery proceeds either via an Eley-Rideal (ER) step with direct H_2O donation or via a Langmuir-Hinshelwood (LH) route via *H formed by the Volmer step [47]. The free-energy profiles for both pathways on Sn (001) and Co_1Sn (001) are compared in Figure 4a. On pristine Sn (001), CO_2 activation to *OCHO along the ER pathway is thermodynamically preferred, which is consistent with the experimentally observed formate selectivity. For both the ER and LH sequences, the RDS is the second proton-coupled electron transfer (PCET). The calculated overpotential requirement corresponds to an applied potential more negative than −0.95 V versus RHE to achieve substantial formate currents, in agreement with the *j*-V behavior in Figure 2b. Introducing a

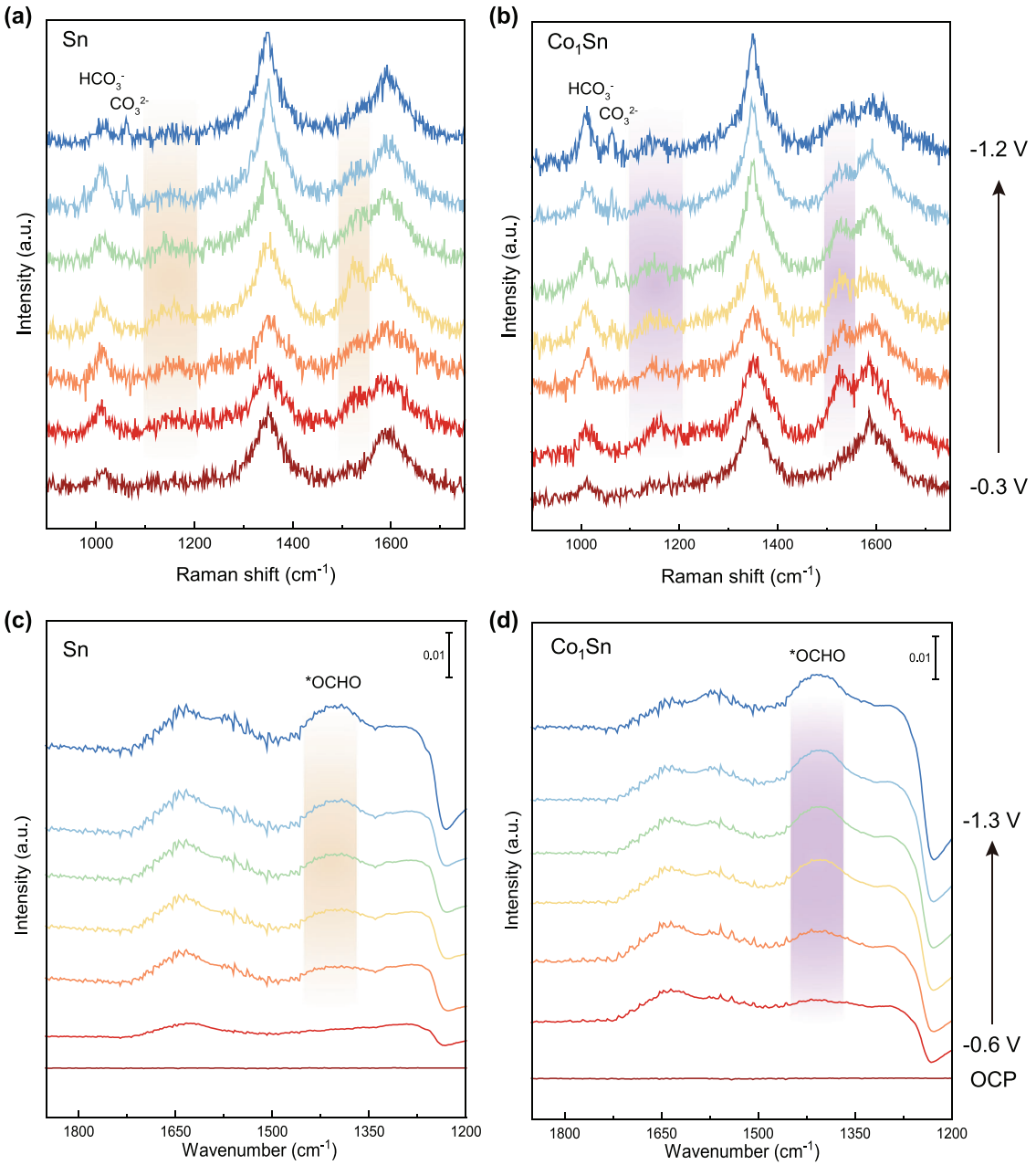

FIGURE 3 | Mechanistic studies of the electrochemical CO_2-to-formate conversion of pristine Sn and Co_1Sn catalysts. (a,b) In situ Raman spectra at different potentials during the CO_2RR. (c,d) In situ ATR-SEIRAS spectra at different potentials during the CO_2RR. Both panels use the same Abs scale and identical processing procedures. All potentials were calibrated to the RHE scale.

single Co atom into the (001) surface adds reactive 3*d* states that strengthen the interaction with CO_2RR intermediates. For Co_1Sn (001), the first electron-transfer step becomes exergonic for both the ER and LH pathways, and the uphill free energy of the RDS for each pathway drops below 0.6 eV. Notably, along the ER route, the second PCET becomes accessible at an applied potential of ∼−0.39 V versus RHE, indicating a substantially lowered kinetic/thermodynamic threshold. The facilitated formation of *COOH on Co_1Sn also rationalizes the slightly earlier onset of CO observed by DEMS (Figure S12). However, the barrier for C-O bond cleavage remains relatively high, so the ER pathway to formate remains dominant under the conditions studied. These trends collectively account for the higher formate productivity measured for Co_1Sn.

Electronic-structure analysis provides a microscopic basis for these effects. The Co single atom introduces an additional density of states (DOS) below the Fermi level and, critically, raises the Sn DOS near the Fermi level (Figure 4b), indicating the activation of adjacent Sn sites by Co. Along the CO_2RR reaction coordinate, the average Sn—Co bond length exhibits an "M-shaped" evolution (Figure 4c; Figure S25), reflecting non-rigid, metal-covalent coupling between the Sn 5*p* and Co 3*d* orbitals. This adaptive "breathing" modulates adsorbate binding strength at different intermediates, enabling simultaneous stabilization of both *COOH (LH pathway) and *OCHO (ER pathway) and mitigation of excessive binding that would otherwise impede turnover. The resulting electronic and geometric flexibility of Co_1Sn (001) provides a coherent explanation for the

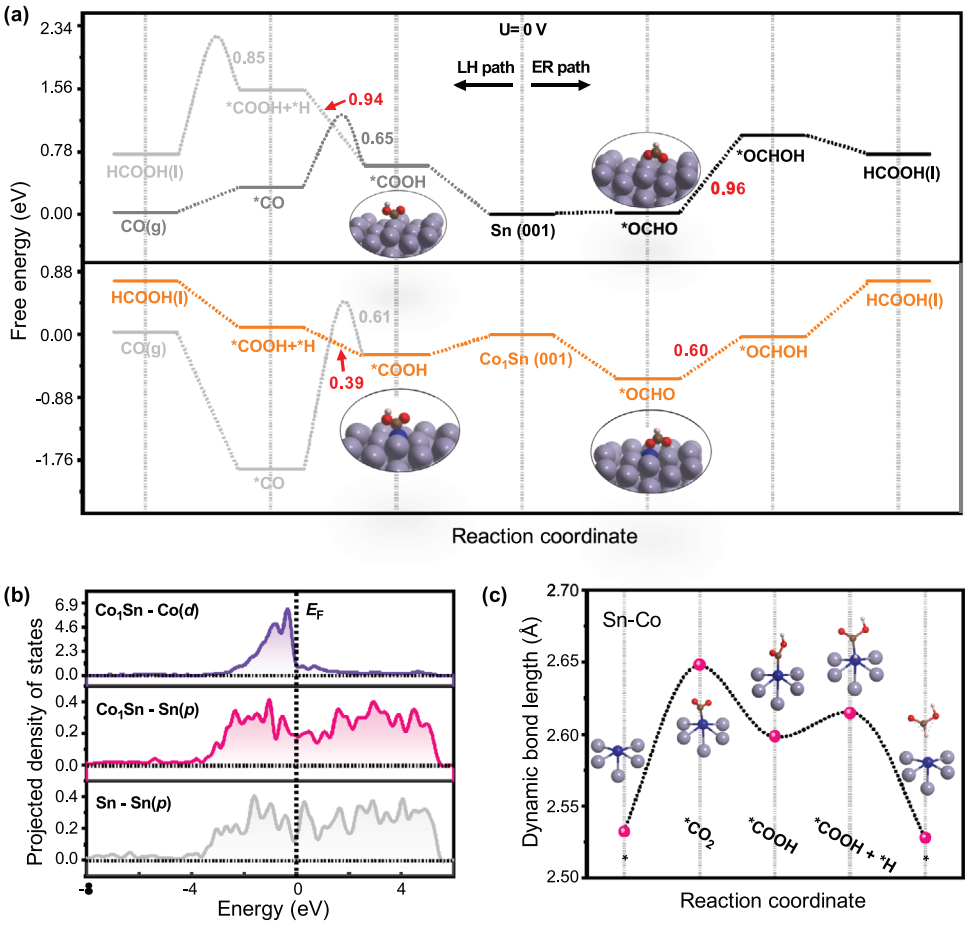

FIGURE 4 | Theoretical calculations. (a) Free energy diagram comparing the CO_2RR processes via different reaction pathways on the Sn and Co_1Sn (001) facets at 0 V versus RHE. The inset shows the ball-stick models of the corresponding intermediates: gray, tin; blue, cobalt; brown, carbon; red, oxygen; pink, hydrogen. (b) Partial density of states (pDOS) projected on Co *d* and Sn *p* orbitals. (c) Dynamic bond length evolution during the CO_2RR along the LH pathway for the Sn—Co bond. The Sn—Co bond evolution of the ER pathway is provided in Figure S25.

experimentally observed combination of a lower overpotential, high formate selectivity, and sustained activity.

3 | Conclusions

We reported a Co_1Sn SAA catalyst in which Co atoms are atomically dispersed within a Sn matrix, enabling highly selective CO_2-to-HCOOH conversion. Unlike pristine Sn, which possesses inferior activity in formate generation and more severe evolution of the HER at large overpotentials, Co_1Sn benefits from Co-induced electronic modulation of the Sn host. The catalyst delivered formate selectivity up to 99% across a broad potential window of −0.83–1.33 V versus RHE. When integrated in a PSE reactor, Co_1Sn sustained >95% FE_{HCOOH} over 130 h of continuous operation at −50 mA cm^{-2}, resulting in the consistent production of pure formic acid. In situ characterization results and theoretical calculations verified that the well-tuned electronic state of Co_1Sn SAA optimized CO_2 activation and the reaction energy barriers for different intermediates, facilitating formate generation in the CO_2RR. Our work establishes single-atom alloying as a rigorous and scalable strategy for rational catalyst design that is readily extendable to other host-dopant combinations.

Author Contributions

The project was conceptualized by C.X. and was supervised by C.X., Y.-P.Z., J.Z., and T.-T.Z. J.X. conducted all the experiments. K.-X.Z. helped with the electrochemical tests. Y.-Z.C., J.-W.L., and X.L. conducted the XAFS simulation analysis. Y.-P.Z. and B.-F.J. performed the DFT calculations. C.-X.L., Q.-X.L., and J.Z. offered guidance in writing the paper. J.X., T.-T.Z., Y.-P.Z., and C.X. wrote the paper with input from all the authors. All the authors discussed the results and commented on the manuscript.

Acknowledgements

The authors acknowledge the National Key Research and Development Program of China (2024YFB4105700), the Scientific Research Innovation Capability Support Project for Young Faculty (SRICSPYF-ZY2025052), CAS Project for Young Scientists in Basic Research (YSBR-051), the National Natural Science Foundation of China (22322201, 22278067, 52273312, 22309200, 22525021 and 22250007), the Natural Science Foundation of Sichuan Province (2025NSFJQ0017) and the University of Electronic Science and Technology of China (ZYGX2025TS001). J. Zeng acknowledges support from the New Cornerstone Science Foundation through the XPLORER PRIZE. The authors thank the Shanghai Synchrotron Radiation Facility of BL11B (https://cstr.cn/31124.02.SSRF.BL11B) for assisting with the XAS measurements. This work was partially carried out at the Instruments Center for Physical Science, University of

Science and Technology of China. This work was also partially carried out at the USTC Center for Micro and Nanoscale Research and Fabrication. The authors also appreciate the Analysis and Testing Center, University of Electronic Science and Technology of China, for their technical support.

Conflicts of Interest

The authors declare no conflicts of interest.

Data Availability Statement

The data that support the findings of this study are available from the corresponding author upon reasonable request.

References

1. J. H. Montoya, L. C. Seitz, P. Chakthranont, A. Vojvodic, T. F. Jaramillo, and J. K. Nørskov, "Materials for Solar Fuels and Chemicals," *Nature Materials* 16 (2017): 70–81, https://doi.org/10.1038/nmat4778.

2. G. A. Olah, G. K. S. Prakash, and A. Goeppert, "Anthropogenic Chemical Carbon Cycle for a Sustainable Future," *Journal of the American Chemical Society* 133 (2011): 12881–12898, https://doi.org/10.1021/ja202642y.

3. J. Y. T. Kim, C. Sellers, S. Hao, T. P. Senftle, and H. Wang, "Different Distributions of Multi-carbon Products in CO_2 and CO Electroreduction under Practical Reaction Conditions," *Nature Catalysis* 6 (2023): 1115–1124, https://doi.org/10.1038/s41929-023-01082-4.

4. H. Shen, H. Jin, H. Li, et al., "Acidic CO_2-to-HCOOH Electrolysis with Industrial-level Current on Phase Engineered Tin Sulfide," *Nature Communications* 14 (2023): 2843.

5. C. Li, M. Guo, B. Yang, et al., "Efficient and Scalable Upcycling of Oceanic Carbon Sources into Bioplastic Monomers," *Nature Catalysis* 8, no. 10 (2025): 1023–1037, https://doi.org/10.1038/s41929-025-01416-4.

6. T. Zheng, C. Liu, C. Guo, et al., "Copper-Catalysed Exclusive CO_2 to Pure Formic Acid Conversion via Single-atom Alloying," *Nature Nanotechnology* 16 (2021): 1386–1393, https://doi.org/10.1038/s41565-021-00974-5.

7. J. Eppinger and K.-W. Huang, "Formic Acid as a Hydrogen Energy Carrier," *ACS Energy Letters* 2 (2016): 188–195, https://doi.org/10.1021/acsenergylett.6b00574.

8. A. Bagger, W. Ju, A. S. Varela, P. Strasser, and J. Rossmeisl, "Electrochemical CO_2 Reduction: a Classification Problem," *Chemphyschem* 18 (2017): 3266–3273, https://doi.org/10.1002/cphc.201700736.

9. C. Peng, S. Yang, G. Luo, et al., "Ampere-Level CO_2-to-formate Electrosynthesis Using Highly Exposed Bismuth(110) Facets Modified with Sulfur-Anchored Sodium Cations," *Chemistry (Weinheim An Der Bergstrasse, Germany)* 9 (2023): 2830–2840, https://doi.org/10.1016/j.chempr.2023.05.008.

10. Y. Shi, Y. Ji, J. Long, et al., *Nature Communications* 11 (2020): 3145.

11. F. Yang, A. O. Elnabawy, R. Schimmenti, et al., "Bismuthene for Highly Efficient Carbon Dioxide Electroreduction Reaction," *Nature Communications* 11 (2020): 1088, https://doi.org/10.1038/s41467-020-14914-9.

12. W. M. Haynes, *CRC Handbook of Chemistry and Physics*, 97th Edition (CRC Press, 2016), https://doi.org/10.1201/9781315380476.

13. Y. Ko, J. Kim, W. H. Lee, et al., "Exploring Dopant Effects in Stannic Oxide Nanoparticles for CO_2 Electro-reduction to Formate," *Nature Communications* 13 (2022): 2205, https://doi.org/10.1038/s41467-022-29783-7.

14. M. Chen, S. Wan, L. Zhong, et al., "Dynamic Restructuring of Cu-Doped SnS_2 Nanoflowers for Highly Selective Electrochemical CO_2 Reduction to Formate," *Angewandte Chemie International Edition* 60 (2021): 26233–26237, https://doi.org/10.1002/anie.202111905.

15. B. Ren, G. Wen, R. Gao, et al., "Nano-crumples Induced Sn-Bi Bimetallic Interface Pattern with Moderate Electron Bank for Highly Efficient CO_2 Electroreduction," *Nature Communications* 13 (2022): 2486, https://doi.org/10.1038/s41467-022-29861-w.

16. S. Zhang, P. Kang, and T. J. Meyer, "Nanostructured Tin Catalysts for Selective Electrochemical Reduction of Carbon Dioxide to Formate," *Journal of the American Chemical Society* 136 (2014): 1734–1737, https://doi.org/10.1021/ja4113885.

17. W. Ma, S. Xie, X.-G. Zhang, et al., "Promoting Electrocatalytic CO_2 Reduction to Formate via Sulfur-boosting Water Activation on Indium Surfaces," *Nature Communications* 10 (2019): 892, https://doi.org/10.1038/s41467-019-08805-x.

18. L. Li, A. Ozden, S. Guo, et al., "Stable, Active CO_2 Reduction to Formate via Redox-modulated Stabilization of Active Sites," *Nature Communications* 12 (2021): 5223, https://doi.org/10.1038/s41467-021-25573-9.

19. F. Liu, X. Ren, J. Zhao, et al., "Inhibiting Sulfur Dissolution and Enhancing Activity of SnS for CO_2 Electroreduction via Electronic State Modulation," *ACS Catalysis* 12 (2022): 13533–13541, https://doi.org/10.1021/acscatal.2c02617.

20. T. Wang, J. Chen, X. Ren, et al., "Halogen-Incorporated Sn Catalysts for Selective Electrochemical CO_2 Reduction to Formate," *Angewandte Chemie International Edition* 62 (2023): 202211174.

21. B. Peng, H. She, Z. Wei, et al., "Sulfur-doping Tunes p-d Orbital Coupling over Asymmetric Zn-Sn Dual-atom for Boosting CO_2 Electroreduction to Formate," *Nature Communications* 16 (2025): 2217, https://doi.org/10.1038/s41467-025-57573-4.

22. Y. Zhang, H. Jang, X. Ge, et al., "Single-Atom Sn on Tensile-Strained ZnO Nanosheets for Highly Efficient Conversion of CO_2 into Formate," *Advanced Energy Materials* 12 (2022): 2202695, https://doi.org/10.1002/aenm.202202695.

23. C. Liang, B. Kim, S. Yang, et al., "High Efficiency Electrochemical Reduction of CO_2 beyond the Two-electron Transfer Pathway on Grain Boundary Rich Ultra-small SnO_2 Nanoparticles," *Journal of Materials Chemistry A* 6 (2018): 10313–10319.

24. W. Luc, C. Collins, S. Wang, et al., "Ag–Sn Bimetallic Catalyst with a Core–Shell Structure for CO_2 Reduction," *Journal of the American Chemical Society* 139 (2017): 1885–1893, https://doi.org/10.1021/jacs.6b10435.

25. J. Xue, X. Dong, C. Liu, et al., "Turning Copper into an Efficient and Stable CO Evolution Catalyst beyond Noble Metals," *Nature Communications* 15 (2024): 5998, https://doi.org/10.1038/s41467-024-50436-4.

26. J. Li, H. Zeng, X. Dong, et al., "Selective CO_2 Electrolysis to CO Using Isolated Antimony Alloyed Copper," *Nature Communications* 14 (2023): 340, https://doi.org/10.1038/s41467-023-35960-z.

27. H. Wei, A. Tan, Z. Xiang, et al., "Modulating p-Orbital of Bismuth Nanosheet by Nickel Doping for Electrocatalytic Carbon Dioxide Reduction Reaction," *Chemsuschem* 15 (2022): 202200752.

28. R. Nankya, Y. Xu, A. Elgazzar, et al., "Cobalt-Doped Bismuth Nanosheet Catalyst for Enhanced Electrochemical CO_2 Reduction to Electrolyte-Free Formic Acid," *Angewandte Chemie International Edition* 63 (2024): 202403671, https://doi.org/10.1002/anie.202403671.

29. J. Li, M. Wei, B. Ji, et al., "Copper-Catalysed Electrochemical CO_2 Methanation via the Alloying of Single Cobalt Atoms," *Angewandte Chemie International Edition* 64 (2025): 202417008, https://doi.org/10.1002/anie.202417008.

30. G. Li, Q. Xu, W. Shi, et al., "Surface States in Bulk Single Crystal of Topological Semimetal $Co_3Sn_2S_2$ toward Water Oxidation," *Science Advances* 5 (2019): aaw9867.

31. G. Cheng, J. D. Carter, and T. Guo, "Investigation of Co Nanoparticles with EXAFS and XANES," *Chemical Physics Letters* 400 (2004): 122–127, https://doi.org/10.1016/j.cplett.2004.10.095.

32. K. Li, J. Xu, T. Zheng, et al., "In Situ Dynamic Construction of a Copper Tin Sulfide Catalyst for High-Performance Electrochemical CO_2

Conversion to Formate," *ACS Catalysis* 12 (2022): 9922–9932, https://doi.org/10.1021/acscatal.2c02627.

33. Y. Jiang, J. Shan, P. Wang, L. Huang, Y. Zheng, and S.-Z. Qiao, "Stabilizing Oxidation State of SnO_2 for Highly Selective CO_2 Electroreduction to Formate at Large Current Densities," *ACS Catalysis* 13, no. 5 (2023): 3101–3108, https://doi.org/10.1021/acscatal.3c00123.

34. X. Wang, F. Li, W.-J. Yin, et al., "Atomically Dispersed Sn Modified with Trace Sulfur Species Derived from Organosulfide Complex for Electroreduction of CO_2," *Applied Catalysis B: Environmental* 304 (2022): 120936, https://doi.org/10.1016/j.apcatb.2021.120936.

35. B. Li, J. Chen, L. Wang, et al., "Dynamic Reconstruction of Cu-doped SnO_2 for Efficient Electrochemical Reduction of CO_2 to Formate," *Applied Catalysis B: Environment and Energy* 363 (2025): 124784, https://doi.org/10.1016/j.apcatb.2024.124784.

36. T.-W. Jiang, X. Qin, K. Ye, et al., "An Interactive Study of Catalyst and Mechanism for Electrochemical CO_2 Reduction to Formate on Pd Surfaces," *Applied Catalysis B: Environmental* 334 (2023): 122815, https://doi.org/10.1016/j.apcatb.2023.122815.

37. L. Xiao, Q. Zheng, S. Luo, et al., *Science Advance* 10 (2024): 2707.

38. Y. Wang, J. Kim, H. D. Jung, et al., "Understanding the First Activation Step of Electrochemical CO_2 Reduction over Ag and Ni-N-C Active Sites," *Nano Energy* 127 (2024): 109728, https://doi.org/10.1016/j.nanoen.2024.109728.

39. I. V. Chernyshova, P. Somasundaran, and S. Ponnurangam, "On the Origin of the Elusive First Intermediate of CO_2 Electroreduction," *Proceedings of the National Academy of Sciences* 115, no. 40 (2018): E9261–E9270, https://doi.org/10.1073/pnas.1802256115.

40. W. Shan, R. Liu, H. Zhao, et al., "In Situ Surface-Enhanced Raman Spectroscopic Evidence on the Origin of Selectivity in CO_2 Electrocatalytic Reduction," *ACS Nano* 14 (2020): 11363–11372, https://doi.org/10.1021/acsnano.0c03534.

41. A. R. Davis and B. G. Oliver, "A Vibrational-spectroscopic Study of the Species Present in the CO_2−H_2O System," *Journal of Solution Chemistry* 1 (1972): 329–339, https://doi.org/10.1007/BF00715991.

42. D. A. Henckel, M. J. Counihan, H. E. Holmes, et al., "Potential Dependence of the Local pH in a CO_2 Reduction Electrolyzer," *ACS Catalysis* 11 (2020): 255–263, https://doi.org/10.1021/acscatal.0c04297.

43. Z. Wang, Y. Li, X. Zhao, et al., "Localized Alkaline Environment via In Situ Electrostatic Confinement for Enhanced CO_2-to-Ethylene Conversion in Neutral Medium," *Journal of the American Chemical Society* 145 (2023): 6339–6348, https://doi.org/10.1021/jacs.2c13384.

44. J. Yin, Z. Gao, F. Wei, et al., "Customizable CO_2 Electroreduction to C_1 or C_{2+} Products through Cu_y/CeO_2 Interface Engineering," *ACS Catalysis* 12 (2022): 1004–1011, https://doi.org/10.1021/acscatal.1c04714.

45. X. Mathew, J. P. Enriquez, C. Mejia-Garcia, et al., "Structural Modifications of SnO_2 Due to the Incorporation of Fe into the Lattice," *Journal of Applied Physics* 100 (2006): 073907, https://doi.org/10.1063/1.2357635.

46. Z. Guo, Y. Yu, C. Li, et al., "Deciphering Structure-Activity Relationship towards CO_2 Electroreduction over SnO_2 by a Standard Research Paradigm," *Angewandte Chemie International Edition* 63 (2024): 202319913, https://doi.org/10.1002/anie.202319913.

47. J. Zhang, C. Zhang, M. Wang, et al., "Isotopic Labelling of Water Reveals the Hydrogen Transfer Route in Electrochemical CO_2 Reduction," *Nature Chemistry* 17 (2025): 334–343, https://doi.org/10.1038/s41557-024-01721-8.

Supporting Information

Additional supporting information can be found online in the Supporting Information section.

Supporting File: adma72719-sup-0001-SuppMat.pdf.